

Noise-free quantum optical frequency shifting driven by mechanics

Linran Fan, Chang-Ling Zou, Menno Poot, Risheng Cheng, Xiang Guo, Xu Han and Hong X. Tang*
Department of Electrical Engineering, Yale University, New Haven, Connecticut 06511, USA

The ability to manipulate single photons is of critical importance for fundamental quantum optics studies and practical implementations of quantum communications. While extraordinary progresses have been made in controlling spatial, temporal, spin and orbit angular momentum degrees of freedom [1–6], frequency-domain control of single photons so far relies on nonlinear optical effects, which have faced obstacles such as noise photons, narrow bandwidth and demanding optical filtering [7–14]. Here we demonstrate the first integrated near-unity efficiency frequency manipulation of single photons, by stretching and compressing a waveguide at 8.3 billion cycles per second. Frequency shift up to 150 GHz at telecom wavelength is realized without measurable added noise and the preservation of quantum coherence is verified through quantum interference between twin photons of different colors. This single photon frequency control approach will be invaluable for increasing the channel capacity of quantum communications and compensating frequency mismatch between quantum systems, paving the road toward hybrid quantum network.

Photons are essential information carriers for quantum communications over long distance, benefiting from low dissipation and decoherence rates at room temperature due to weak interactions with environment. While unitary operations of single photons on temporal, spatial and polarization domains can be readily realized with passive photonic devices [1–4], frequency control requires active photonic devices to change photon energy, which are challenging due to the weak photon-photon interaction [7–14]. Nonetheless, frequency control of single photons plays a central role for a wide range of quantum technologies [9–15]. It provides an efficient approach to encode quantum information through frequency multiplexing, thus can boost quantum channel capacity [15]. In addition, the frequency control of single photons is indispensable to bridge different quantum systems. Frequency mismatch resulting from disparate qubit systems [16], qubit inhomogeneity [17] and qubit spectrum diffusion [18], can be resolved through frequency manipulation.

Typically, single photon frequency conversion is realized with nonlinear optical processes [7–14] and effective nonlinear optical effects mediated by intermediate excitations [19, 20]. Because of the inherent weak photon-photon interaction in dielectrics, strong optical pump fields are required to stimulate the frequency conversion

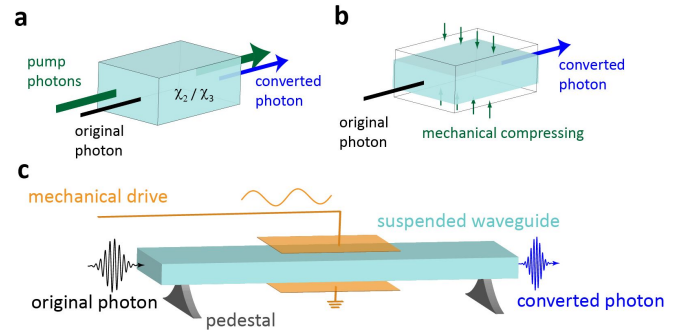


Figure 1. **Principles of quantum frequency conversion.** **a.** Frequency conversion using nonlinear optical processes. **b.** Frequency conversion induced by the mechanical deformation. During the photon’s propagation, the medium is compressed or stretched rapidly, causing frequency shift of the photon. **c.** Schematic of a suspended waveguide made of piezoelectric material. The co-localization of the mechanical and optical modes in the waveguide leads to strong optomechanical interaction, and the piezoelectric effect provides the efficient interface to control the mechanical motion using RF signals.

[7–14]. Therefore, high-performance optical filtering at single photon levels is essential to separate signals from strong optical pump fields and noise photons generated through undesired nonlinear optical effects such as Raman and fluorescence [21]. Moreover, noise photons in the same spectrum range with signals cannot be filtered. Also, the frequency conversion based on nonlinear optical processes can only work at certain wavelengths with limited bandwidth, due to the stringent momentum and energy conservation conditions [8–14].

In this Letter, we realize frequency manipulation of single photons through controlling the mechanical motion of a waveguide. By resonantly stretching a waveguide at 8.3 GHz, we demonstrate frequency shifting of single photons with near-unity intrinsic efficiency in a fully integrated device. High-visibility quantum interference between twin photons with different colors is observed, indicating the quantum coherence conservation. The noise during the conversion process is also found to be below measurable level.

The principle of conventional frequency conversion based on nonlinear optical processes is illustrated in Fig. 1a, where input photons are mixed with pump photons in nonlinear optical material to generate output photons at another frequency. Figure 1b explains our approach using mechanical deformation. The mechanical deformation changes optical length, leading to compres-

sion or stretching of photons, which results in frequency shift. In contrast to multi-wave mixing in Fig. 1a, the frequency conversion induced by the mechanical deformation does not require optical pumps, thus noise generation mechanisms arising from high intensity optical pump are eliminated. This process can also be realized with electro-optic effect, and here the frequency shift induced by mechanics can be further enhanced by the mechanical resonance. In the adiabatic limit where the mechanical change rate is much smaller than the optical frequency ω_o , the frequency shift $\delta\omega$ is proportional to the mechanical deformation δx

$$\delta\omega \approx -v_g k_o \frac{\partial n_{\text{eff}}}{\partial x} \delta x, \quad (1)$$

where k_o , v_g and n_{eff} are the photon vacuum wavevector, the group velocity and the effective refractive index respectively (Supplementary Section I). In such an adiabatic process, the adiabatic invariant is the photon number, thus photons can be converted with unity efficiency [22, 23]. Adiabatic frequency shifting has also been demonstrated in optical micro-cavities based on refractive index modulation through carrier injection [23–25]. Although impressive progresses have been achieved, the cavity-based structure and carrier-injection mechanism are still in need of significant improvement to overcome their limits in efficiency, noise and bandwidth.

To implement the mechanical adiabatic frequency shifting, we use a suspended waveguide made of piezoelectric material, which provides efficient, high amplitude actuation of mechanical motion through RF signals (Fig. 1c) [26]. The mechanical thickness mode of the suspended waveguide is used for its high oscillation frequency and strong interaction with the transverse-magnetic (TM) optical mode (Fig. 2a). Following the mechanical vibration, the effective refractive index changes periodically. Thus photons in the waveguide experience different optical length changes with different drive phase ϕ with respect to the photon arrival time. The corresponding frequency shift can be expressed as

$$\delta\omega = -v_g k_o \frac{\partial n_{\text{eff}}}{\partial x} \delta X \left[\sin\left(\phi - \frac{\omega_m L}{2v_g}\right) - \sin\left(\phi + \frac{\omega_m L}{2v_g}\right) \right], \quad (2)$$

where ω_m is the angular frequency of the mechanical mode, δX is the mechanical motion amplitude, and L is the waveguide length (Supplementary Section I). In order to avoid spectral distortion, the photon duration τ should be much smaller than the mechanical oscillation period $2\pi/\omega_m$. In Fig. 2b, we compare the simulated output spectrum of a Gaussian input photon with different τ and ϕ . As predicted by equation 2, $\delta\omega$ follows a sinusoidal dependence on ϕ for short photon duration. The maximum frequency shift and minimum shape distortion happen at $\phi = 0$ and $\phi = \pi$, where the refractive index change is largest and most uniform. With a very short

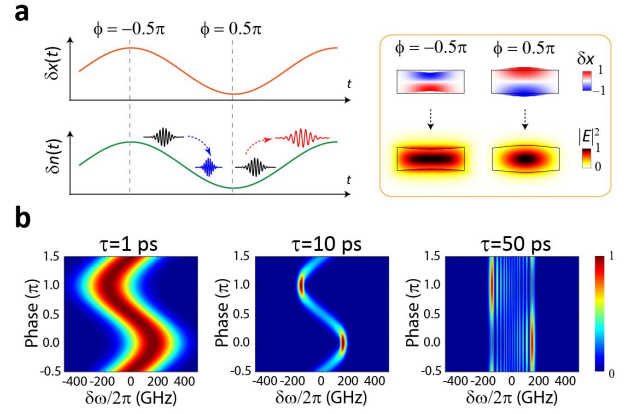


Figure 2. Frequency conversion induced by the mechanical motion. **a.** With different mechanical oscillation phases ϕ , photons experience different refractive index changes, and thus different frequency shift directions and amplitudes. The mechanical thickness mode and TM optical mode of a rectangular waveguide cross-section are shown. The positive (negative) displacement leads to the increase (decrease) of effective refractive index change. **b.** Simulated output spectrum of a Gaussian input photon (i.e. $a(t) = e^{-i\omega_o(t-t_0)^2/\tau^2}$) (Supplementary section I). The parameters used are the waveguide length $L = 5$ mm, the refractive index modulation depth $\delta n_{\text{eff}}/n = 5 \times 10^{-4}$, and the mechanical frequency $\omega_m/2\pi = 8.3$ GHz, the group index of TM optical mode $n = 2$ and the optical frequency $\omega_o/2\pi = 194$ THz. Different photon durations τ of 1 ps, 10 ps and 50 ps are shown.

photon duration, the photon spectrum remains Gaussian. When the photon duration becomes comparable to the mechanical oscillation period, sidebands are generated and the photon spectrum is distorted due to the nonlinear refractive index change.

In experiment, the frequency shifting device is fabricated from an aluminum nitride (AlN) layer on a silicon dioxide (SiO₂) cladding on silicon (Si) wafer (Fig. 3a and further explained in Methods). The AlN thickness is 650 nm, resulting in a fundamental thickness mode frequency of $\omega_m/2\pi = 8.26$ GHz (Fig. 3d). The waveguide is 6 mm long, folded into a meander with a footprint of 1 mm². The RF ground and signal electrodes are situated close to the waveguide, on the AlN and Si layers respectively to produce strong driving electrical fields (Fig. 3b). The waveguide width is intentionally widened slightly every 100 μm as shown in Fig. 3c, where a point-like pedestal can be formed [26]. The pedestal is reduced to around 100×100 nm² in size to minimize the clamping loss, while remaining robust to support the suspended waveguide. In this way, a mechanical quality factor over 2000 is achieved at room temperature (Fig. 3d).

The device is first tested with photons produced through spontaneous parametric down conversion (SPDC) with a centre wavelength 1554.0 nm, and the output photon spectrum is measured by a superconduct-

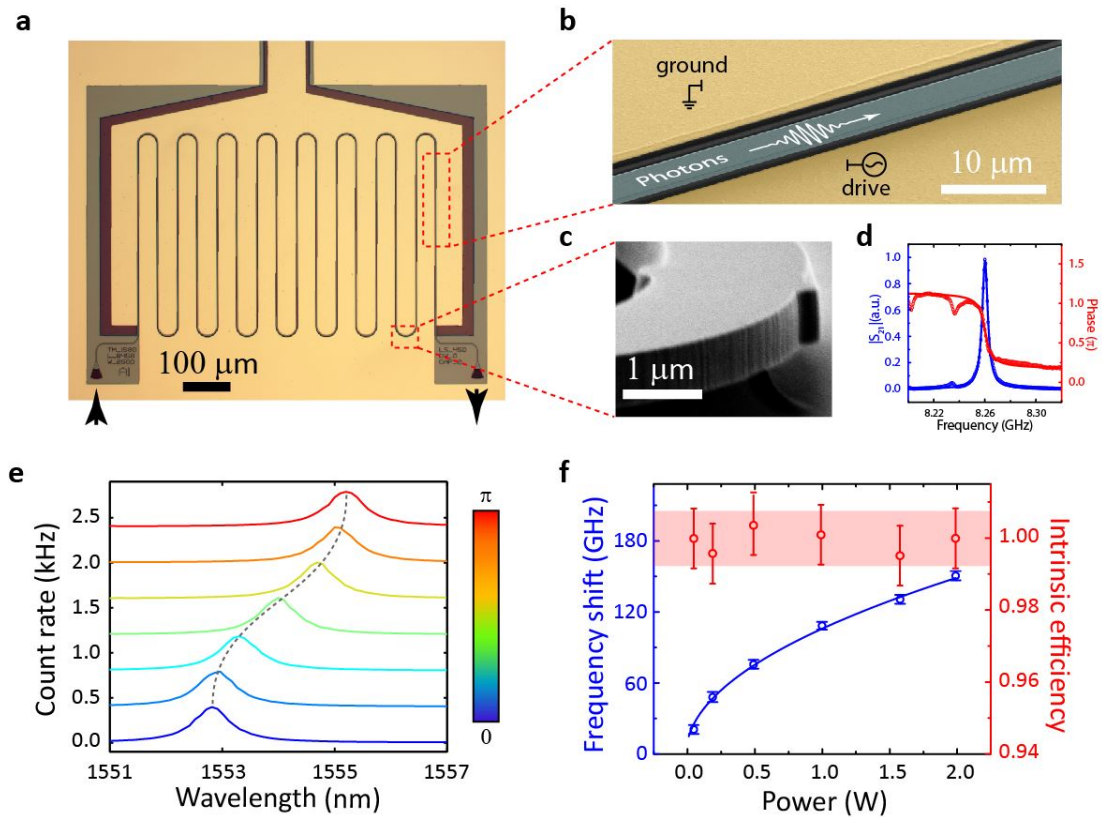


Figure 3. **Single photon frequency control.** **a.** Optical image of the suspended AlN waveguide. The waveguide is 6 mm in length, folded into a meander within $1 \times 1 \text{ mm}^2$. **b.** Scanning electron microscope (SEM) image of the device in false color. The waveguide (cyan) is $2.4 \mu\text{m}$ wide. The horizontal distance between the two RF electrodes (yellow) and the waveguide are 100 nm and 800 nm respectively. The two RF electrodes are deposited on top of the AlN and Si layers respectively. **c.** SEM image at a supporting point of the waveguide. The waveguide width is increased by 200 nm, and a pedestal with $100 \times 100 \text{ nm}^2$ size can be formed to support the waveguide. **d.** Driven response of the mechanical thickness mode with a fit to extract the mechanical quality factor. **e.** Single photon spectrum measured using SSPD with an optical bandpass filter. The dotted grey line shows the theoretical centre wavelength shift (equation 2). The curves are offset for clarity. **f.** Frequency shift amplitude (blue) and intrinsic conversion efficiency (red) dependence on the RF drive power. The solid blue line is the fitted frequency shift with square-root dependence on the drive power. The shaded area indicates the unity intrinsic conversion efficiency, measured with reference to the photon counting rate without the RF drive. The error of the frequency shift is estimated based on the fitting of the measured spectrum. The error of the intrinsic conversion efficiency is estimated based on the Poisson distribution of photon counting.

ing single-photon detector (SSPD) with a 0.3 nm optical bandpass filter. The RF drive is synchronized with the photon arrival time to obtain steady RF phase ϕ (Supplementary Section II). The photon spectrum is shifted without spectral distortion (Fig. 3e). By changing ϕ from 0 to π with fixed drive power 2 W, the centre wavelength is shifted from 1552.8 nm to 1555.2 nm, corresponding to a maximum frequency shift $\pm 2\pi \times 150 \text{ GHz}$. The frequency shift has a sinusoidal dependence on ϕ , which agrees with the prediction of equation 2. Beside the drive phase, $\delta\omega$ can be precisely controlled by the drive power as well (Fig. 3f). Since the frequency shift is proportional to the amplitude of the mechanical displacement (equation 2), which in turn is proportional to the square root of the drive power P , we have the frequency shift

coefficient $\eta = \frac{\delta\omega}{\sqrt{P}} \approx 2\pi \times 106.8 \text{ GHz}/\sqrt{\text{W}}$. The intrinsic conversion efficiency can be estimated by comparing the total count rates under different RF drive power with the count rate under no RF drive (Fig. 3f). No statistically significant change of count rates is observed, indicating the near-unity intrinsic conversion efficiency for single photons.

In order to examine the quantum coherence of the conversion process, we carried out the quantum interference experiment with non-degenerate photon pairs (Fig. 4a) [27]. Twin photons with neglectable spectral correlations respectively centered at 1551.1 nm (referred to as blue photon) and 1551.9 nm (referred to as red photon) are generated through type-II SPDC (Supplementary Section III). The blue and red photons pass through an op-

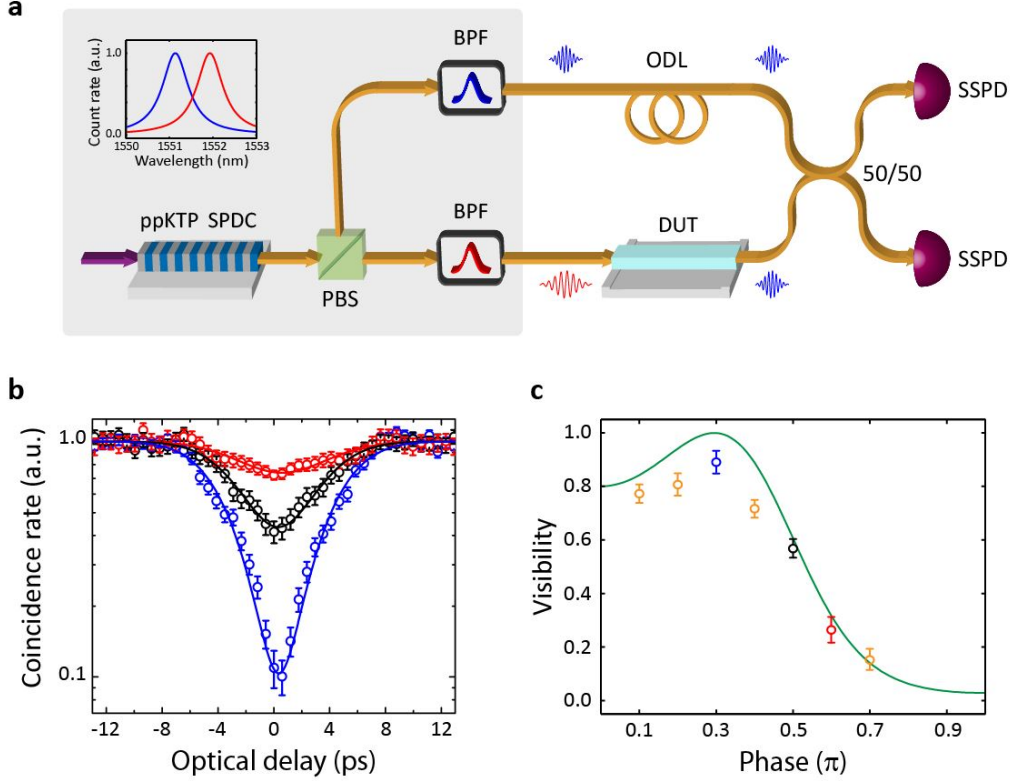


Figure 4. **Two photon quantum interference with different colors.** **a.** Experimental setup for two-photon quantum interference with different colors. ppKTP, periodically-poled potassium titanyl phosphate; PBS, polarizing beam splitter; BPF, optical bandpass filter; ODL, optical delay line; DUT, device under test; SSPD, superconducting single-photon detector. **b.** Coincidence rate between the two SSPDs normalized by the coincidence rate at an optical delay much larger than the photon duration, for unshifted photons (black), red-shifted photons (red) and blue-shifted photons (blue). **c.** Visibility dependence (symbols) on the RF drive phase. The black, red and blue symbols correspond to the black, red and blue curves in **b** respectively. Theoretical visibility (solid line) for different phases with a frequency shift amplitude of 150 GHz, other parameters are the initial frequency separation (100 GHz) and the photon duration ($\tau = 4$ ps). The error is estimated based on the poisson distribution of photon counting.

tical delay line and the device respectively. Then the photons are coupled into a 50/50 beam splitter, and detected by two SSPDs. The coincidence rate is calculated by comparing the arrival time lists of the two SSPDs, and normalized with the coincidence rate at the optical delay much larger than the photon coherence time (Fig. 4b). Without applying the RF drive, we observe a dip in the coincidence with a visibility $V = (56.1 \pm 3.1)\%$ by fitting the coincidence rate with the function

$$C = 1 - Ve^{-\frac{t^2}{2\tau^2}}, \quad (3)$$

where C is the normalized coincidence rate, V is the visibility, t is the delay time, and τ is the pulse duration of single photons [28]. By blue-shifting the red photons, the highest visibility $V = (90.3 \pm 4.6)\%$ can be reached when the spectra of the two photons overlap. In contrast, the visibility is reduced by red-shifting the red photons, indicating the further separation of the photons in frequency domain. As shown in Fig. 3e, the centre wave-

length of photons can be controlled by tuning the drive phase ϕ . Therefore, we can change the indistinguishability between the two photons continuously via the phase ϕ (Fig. 4c).

The high visibility of the quantum interference confirms the preservation of quantum coherence. In order to further verify the noise performance, we also measure the dark count rate of SSPD and the total noise count rate without input photons and optical filters, which are 42.54 ± 0.38 Hz and 42.39 ± 0.38 Hz respectively. No statistically significant amount of noise photons from the frequency shifting are measured. Moreover, the frequency shifting requires no phase matching conditions, therefore suitable for broadband quantum communication (Supplementary section II). Compared with bulk electro-optic materials such as LiNbO_3 , the small footprint, scalability, low insertion loss and CMOS compatibility make our device easy to integrate into quantum networks. (Supplementary section IV). Further improvements in frequency

shift range can be readily achieved through integrating more devices on a single chip, as well as increasing mechanical quality factors by reducing the operation temperature.

In conclusion, we have demonstrated the frequency manipulation of single photons by controlling the mechanical motion of integrated AlN waveguides. With strong optomechanical interaction and piezoelectric actuation, we have been able to shift single photon frequency over 300 GHz at telecom wavelength with near-unity intrinsic efficiency and no added noise, while preserving the quantum coherence of single photons. As no optical pump or phase matching is required in this process, our results provide an efficient and clean solution for the single photon frequency control. This paves the way to realize the high-capacity quantum communications between different quantum systems, pushing forward the frontier of quantum technology.

Note added: Upon submission of this manuscript, we became aware of the work by Wright *et al.*, where single photon frequency shifting is realized based on electro-optic effect [29].

Methods

Device fabrication. The device is fabricated from 650-nm-thick AlN on SiO₂ (thickness 2.2 μm) on a Si wafer. Optical waveguides are patterned with electron beam lithography (EBL) using hydrogen silsesquioxane (HSQ) resist, subsequently transferred to the AlN layer by chlorine-based reactive ion-etching (RIE). In this step, only 500 nm out of the 650 nm AlN is initially etched. In a second EBL using ZEP520A resist, the release window is defined, and followed by RIE of the remaining 150 nm AlN. A fluorine-based deep RIE is used to selectively etch the SiO₂ exposed by the release window down to the silicon substrate. A third EBL is performed to define the RF electrodes in polymethyl methacrylate (PMMA). After development, 300 nm gold is thermally evaporated, followed by lift-off in acetone. Finally, the waveguides are released in buffered oxide etchant. By timing the releasing process, the whole waveguide is suspended, only supported by specifically engineered pedestals (Fig. 3c).

Acknowledgments

We acknowledge funding support from an LPS/ARO grant (W911NF-14-1-0563), AFOSR MURI grant (FA9550-15-1-0029), and DARPA ORCHID program through a grant from the Air Force Office of Scientific Research (AFOSR FA9550-10-1-0297), and the Packard Foundation. Facilities used were supported by Yale Institute for Nanoscience and Quantum Engineering and NSF MRSEC DMR 1119826. The authors thank Michael Power and Dr. Michael Rooks for assistance in device fabrication.

Author contributions

H.X.T., L.F. & C.-L.Z. conceived the experiment; L.F., R.C. & X.H. fabricated the device; L.F., M.P., R.C. & X.G. performed the measurements; L.F. & C.-L.Z. analyzed the data. L.F. & C.-L.Z. wrote the manuscript, and all authors contribute to the manuscript. H.X.T. supervised the work.

Additional information

Supplementary information is available in the online version of the paper. Reprints and permissions information is available online at www.nature.com/reprints. Correspondence and requests for materials should be addressed to H.X.T.

Competing financial interests

The authors declare no competing financial interests.

* hong.tang@yale.edu

- [1] Bliokh, K. Y., Rodríguez-Fortuño, F. J., Nori, F. & Zayats, A. V. Spin-orbit interactions of light. *Nature Photon.* 9, 796-808 (2015).
- [2] Shadbolt, P. J., Verde, M. R., Peruzzo, A., Politi, A., Laing, A., Lobino, M., Matthews, J. C., Thompson, M. G. & O'Brien, J. L. Generating, manipulating and measuring entanglement and mixture with a reconfigurable photonic circuit. *Nature Photon.* 6, 45-49 (2012).
- [3] Spring, J. B., Metcalf, B. J., Humphreys, P. C., Kolthammer, W. S., Jin, X. M., Barbieri, M., Datta, A., Thomas-Peter, N., Langford, N. K., Kundys, D., Gates, J. C., Smith, B. J., Smith, P. G. R., & Walmsley, I. A. Boson sampling on a photonic chip. *Science* 339, 798-801 (2013).
- [4] Marcikic, I., De Riedmatten, H., Tittel, W., Zbinden, H., Legré, M., & Gisin, N. Distribution of time-bin entangled qubits over 50 km of optical fiber. *Phys. Rev. Lett.* 93, 180502, (2004).
- [5] Ferdous, F., Miao, H., Leaird, D. E., Srinivasan, K., Wang, J., Chen, L., Varghese, L. T. & Weiner, A. M. Spectral line-by-line pulse shaping of on-chip microresonator frequency combs. *Nature Photon.* 5, 770-776 (2011).
- [6] Franson, J. D. Bell inequality for position and time. *Phys. Rev. Lett.* 62, 2205 (1989).
- [7] Kumar, P. Quantum frequency conversion. *Opt. Lett.* 15, 1476-1478 (1990).
- [8] Salem, R., Foster, M. A., Turner, A. C., Geraghty, D. F., Lipson, M. & Gaeta, A. L. Signal regeneration using low-power four-wave mixing on silicon chip. *Nature Photon.* 2, 35-38 (2008).
- [9] McGuinness, H. J., Raymer, M. G., McKinstrie, C. J., & Radic, S. Quantum frequency translation of single-photon states in a photonic crystal fiber. *Phys. Rev. Lett.* 105, 093604 (2010).
- [10] Rakher, M. T., Ma, L., Slattery, O., Tang, X., & Srinivasan, K. Quantum transduction of telecommunications-band single photons from a quantum dot by frequency upconversion. *Nature Photon.* 4, 786-791 (2010).
- [11] Ikuta, R., Kusaka, Y., Kitano, T., Kato, H., Yamamoto, T., Koashi, M., & Imoto, N. Wide-band quantum interface for visible-to-telecommunication wavelength conver-

- sion. *Nature Comm.* 2, 1544 (2011).
- [12] De Greve, K., Yu, L., McMahon, P. L., Pelc, J. S., Natarajan, C. M., Kim, N. Y., Abe, E., Maier, S., Schneider, C., Kamp, M. & Höfling, S. Quantum-dot spin-photon entanglement via frequency downconversion to telecom wavelength. *Nature* 491, 421–425 (2012).
- [13] Zaske, S., Lenhard, A., Kefler, C. A., Kettler, J., Hepp, C., Arend, C., Albrecht, R., Schulz, W. M., Jetter, M., Michler, P. & Becher, C. Visible-to-telecom quantum frequency conversion of light from a single quantum emitter. *Phys. Rev. Lett.* 109, 147404 (2012).
- [14] Clark, A. S., Shahnia, S., Collins, M. J., Xiong, C., & Eggleton, B. J. High-efficiency frequency conversion in the single-photon regime. *Opt. Lett.* 38, 947-949 (2013).
- [15] Sinclair, N., Saglamyurek, E., Mallahzadeh, H., Slater, J. A., George, M., Ricken, R., Hedges, M. P., Oblak, D., Simon, C., Sohler, W. & Tittel, W. Spectral multiplexing for scalable quantum photonics using an atomic frequency comb quantum memory and feed-forward control. *Phys. Rev. Lett.* 113, 053603 (2014).
- [16] Gao, W. B., Imamoglu, A., Bernien, H. & Hanson, R. Coherent manipulation, measurement and entanglement of individual solid-state spins using optical fields. *Nature Photon.* 9, 363-373 (2015).
- [17] Reithmaier, J. P., Sek, G., Löffler, A., Hofmann, C., Kuhn, S., Reitzenstein, S., Keldysh, L. V., Kulakovskii, V. D., Reinecke, T. L. & Forchel, A. Strong coupling in a single quantum dot-semiconductor microcavity system. *Nature*, 432, 197-200 (2004).
- [18] Sallen, G., Tribu, A., Aichele, T., André, R., Besombes, L., Bougerol, C., Richard, M., Tatarenko, S., Kheng, K. & Poizat, J. P. Subnanosecond spectral diffusion measurement using photon correlation. *Nature Photon.* 4, 696-699 (2010).
- [19] Hill, J. T., Safavi-Naeini, A. H., Chan, J. & Painter, O. Coherent optical wavelength conversion via cavity optomechanics. *Nature comm.* 3, 1196 (2012).
- [20] Liu, Y., Davanço, M., Aksyuk, V., & Srinivasan, K. Electromagnetically induced transparency and wideband wavelength conversion in silicon nitride microdisk optomechanical resonators. *Phys. Rev. Lett.* 110, 223603 (2013).
- [21] Kuo, P. S., Pelc, J. S., Slattery, O., Kim, Y. S., Fejer, M. M., & Tang, X. Reducing noise in single-photon-level frequency conversion. *Opt. Lett.* 38, 1310-1312 (2013).
- [22] Fariás, D. A. & Eckstein, J. N. Coupled-mode analysis of an electrooptic frequency shifter. *IEEE J. Quant Electron.* 39, 358-363 (2003).
- [23] Notomi, M. Manipulating light with strongly modulated photonic crystals, *Reports Prog. Phys.* 73, 096501 (2010).
- [24] Preble, S. F., Xu, Q. & Lipson, M. Changing the colour of light in a silicon resonator. *Nature Photon.* 1, 293 - 296 (2007).
- [25] Tanabe, T., Notomi, M., Taniyama, H. & Kuramochi, E. Dynamic release of trapped light from an ultrahigh-Q nanocavity via adiabatic frequency tuning. *Phys. Rev. Lett.* 102, 043907 (2009).
- [26] Fan, L., Fong, K. Y., Poot, M. & Tang, H. X. Cascaded optical transparency in multimode-cavity optomechanical systems. *Nature Comm.* 6, 5850 (2015).
- [27] Hong, C. K., Ou, Z. Y., & Mandel, L. Measurement of subpicosecond time intervals between two photons by interference. *Phys. Rev. Lett.*, 59, 2044 (1987).
- [28] Bachor, H. A. & Ralph, T. C. A guide to experiments in quantum optics, Wiley-VCH (2004).
- [29] Wright, L. J., Karpinski, M., Soller, C. & Smith B. J. Spectral shearing of quantum light pulses by electro-optic phase modulation. arXiv:1605.00640 <<http://arxiv.org/abs/1605.00640>> (2016).

SUPPLEMENTARY INFORMATION

I. THEORY OF FREQUENCY SHIFTING

For an optical pulse $a(z, t)e^{i\beta z - i\omega_0 t}$ propagating long z -direction with centre frequency ω_0 and wave-vector β , the pulse propagation equation can be written as [S1]

$$\frac{\partial a(z, t)}{\partial z} + \frac{1}{v_g} \frac{\partial a(z, t)}{\partial t} = i\delta\beta(z, t)a(z, t), \quad (\text{S.1})$$

where v_g is the group velocity, $\delta\beta$ is the wave-vector change due to external perturbation. For the effective refractive index change due to harmonically driven mechanical deformation, we have

$$\delta\beta(z, t) = \delta n_{\text{eff}} k_0 \sin(\omega_m t + \varphi) \Pi(z/L), \quad (\text{S.2})$$

where δn_{eff} is the change of effective refractive index, k_0 is the vacuum wavevector, ω_m is the driving angular frequency, and φ is the mechanical oscillation phase, L is the waveguide length, and $\Pi(x)$ is the rectangular function, i.e. $\Pi(x) = 0$ for $|x| > \frac{1}{2}$ and $\Pi(x) = 1$ for $|x| < \frac{1}{2}$. If we define two new arguments $\xi = t + \frac{z}{v_g}$ and $\eta = t - \frac{z}{v_g}$, then equation S.1 becomes

$$\frac{\partial a(\xi, \eta)}{\partial \xi} = i \frac{v_g}{2} \delta\beta(\xi, \eta) a(\xi, \eta), \quad (\text{S.3})$$

which is directly integrable

$$a(\xi, \eta) = g(\eta) \exp \left[i \frac{v_g}{2} \int_{\eta}^{\xi} \delta\beta(x, \eta) dx \right], \quad (\text{S.4})$$

where $g(\eta)$ is determined by the initial photon waveform. Using equation S.2, we have

$$\int_{\eta}^{\xi} \delta\beta(x, \eta) dx = \int_{\eta}^{\xi} \delta n_{\text{eff}} k_0 \sin(\omega_m \frac{x + \eta}{2} + \varphi) \Pi(\frac{x - \eta}{2\tau_p}) dx \quad (\text{S.5})$$

where $\tau_p = L/v_g$ denotes the pulse propagation time in the waveguide. For $z = L/2$ at the output port, we have

$$a(\frac{L}{2}, t) = g(t - \frac{\tau_p}{2}) \exp \left\{ -i v_g \frac{\delta n_{\text{eff}} k_0}{\omega_m} \left[\cos(\omega_m t + \varphi) - \cos \left[\omega_m (t - \frac{\tau_p}{2}) + \varphi \right] \right] \right\}. \quad (\text{S.6})$$

And for $z = -L/2$ at the input port, we have

$$a(-\frac{L}{2}, t) = g(t + \frac{\tau_p}{2}) \exp \left\{ -i v_g \frac{\delta n_{\text{eff}} k_0}{\omega_m} \left[\cos(\omega_m t + \varphi) - \cos \left[\omega_m (t + \frac{\tau_p}{2}) + \varphi \right] \right] \right\}. \quad (\text{S.7})$$

Therefore, we obtain the relation between output and input pulses

$$a(\frac{L}{2}, t) = a(-\frac{L}{2}, t - \tau_p) \exp \left\{ -i v_g \frac{\delta n_{\text{eff}} k_0}{\omega_m} \left[\cos(\omega_m t + \varphi) - \cos(\omega_m (t - \tau_p) + \varphi) \right] \right\}. \quad (\text{S.8})$$

If the pulse duration is much smaller than the period of the mechanical oscillation, i.e. $|t - t_e| \ll \tau_p$ with t_e the time when photon exits the waveguide, the frequency shift can be approximated as

$$a(\frac{L}{2}, t) \approx a(-\frac{L}{2}, t - \tau_p) \exp(-i\delta\omega t + \psi) \quad (\text{S.9})$$

$$\delta\omega = -v_g k_0 \delta n_{\text{eff}} \left[\sin(\phi - \frac{\omega_m L}{2v_g}) - \sin(\phi + \frac{\omega_m L}{2v_g}) \right] \quad (\text{S.10})$$

where $\phi = \omega_m t_e + \varphi - \frac{\omega_m \tau_p}{2}$ and $\Phi = v_g \frac{\delta n_{\text{eff}} k_0}{\omega_m} \left[\cos(\omega_m t_e + \phi + \frac{\omega_m L}{2v_g}) - \cos(\omega_m t_e + \phi - \frac{\omega_m L}{2v_g}) \right]$.

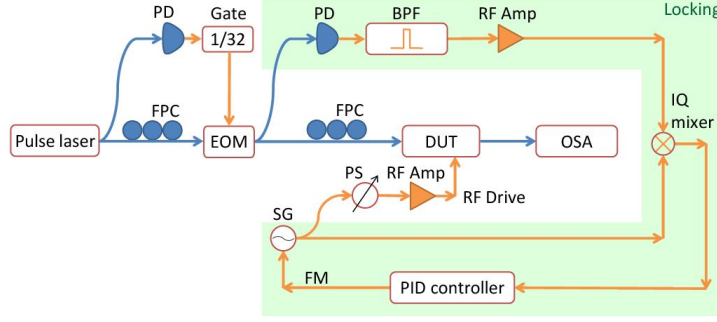


Figure S1. **The experimental setup to realize frequency shifting for optical pulses.** FPC, fiber polarization controller; PD, photodetector; EOM, electro-optical modulator; Gate, square wave gate voltage; DUT, device under test; OSA, optical spectrum analyzer; BPF, bandpass filter; RF Amp, RF amplifier; FM, frequency modulator; SG, signal generator; PS, phase shifter.

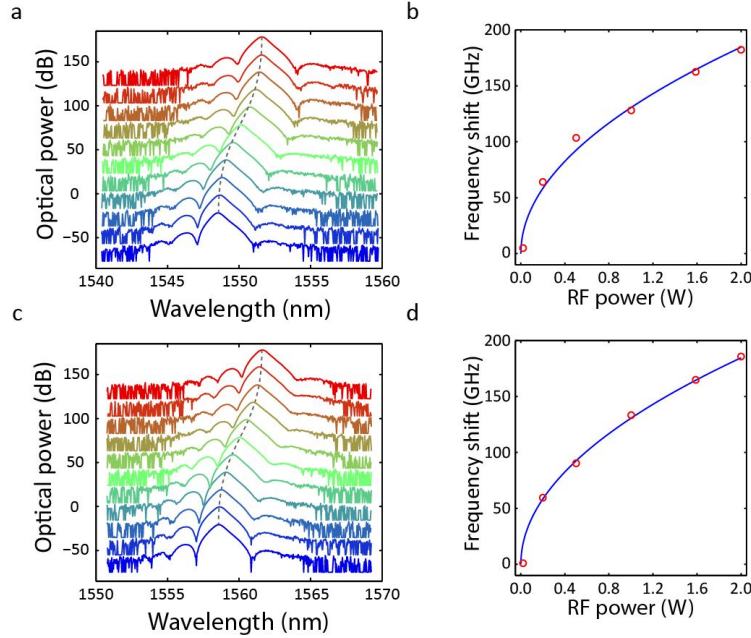


Figure S2. **Frequency shift for optical pulses.** The optical spectrum after frequency shifting with 1550 nm (a) and 1560 nm (c) input photons is displayed. The phase shifter is tuned from 0 to π (blue to red). The dotted grey line shows the theoretical centre wavelength shift. The frequency shift for both 1550 nm (b) and 1560 nm (d) photons is proportional to the square root of the RF drive power.

II. DEVICE CHARACTERIZATION IN THE CLASSICAL REGIME

The experimental setup to realize frequency shifting of optical pulses is displayed in Fig. S1. We used a mode-lock laser with 48.6 MHz repetition rate and 4 ps photon duration. First, the repetition rate is decreased to 1.52 MHz by applying gate voltage to an electro-optical modulator (EOM). The output from the EOM is divided into two parts. The first part is sent into the device, and then the optical spectrum analyzer to monitor the frequency shift. The second part is sent directly into a high frequency photo-detector. The optical pulses are short enough to generate high frequency harmonics of the fundamental 1.52 MHz signal from the photo-detector. One high-order harmonic signal from the photo-detector is mixed with the RF drive for the mechanical thickness mode. The mixed signal is used as the feedback for the RF drive through a PID controller. In this way, the RF drive is synchronized to the

optical pulses from the mode-lock laser, and the jitter between the arrival time of optical pulses and RF drive can be controlled below 2 ps, which is much smaller than the mechanical mode period (~ 120 ps). By synchronizing the RF drive to different order harmonics of optical pulse, the RF drive can be stepped by 1.52 MHz, which is fine enough to match the mechanical resonance (FWHM=4.13 MHz). The synchronized RF drive is then sent into the device with adjustable phase and maximum power 33 dBm.

The centre wavelength of the input optical pulses is set to be 1550 nm. The measured optical power spectrum after the frequency shifting with different phase between optical pulses and RF drive is displayed in Fig. S2a. The maximum frequency shift of 180 GHz is observed on both the red and blue sides. As the mechanical mode displacement is proportional to the driving electric field strength, the frequency shift amplitude is proportional to the square root of the RF drive power as shown in Fig. S2b. The fitting of data gives the shifting coefficient $\eta = \frac{\delta f}{\sqrt{P}} \approx 130.8 \text{ GHz}/\sqrt{W}$, where P is the RF drive power. Then the centre wavelength of the input optical pulses is set to be 1560 nm. Similar performance is observed with the 1560 nm input optical pulses (Fig. S2c & d).

III. EXPERIMENTAL SETUP FOR TWO-PHOTON QUANTUM INTERFERENCE WITH DIFFERENT COLORS

The single-photon characterization of the frequency shifting is realized with the setup shown in Fig. S3 [S2]. Strong 1550 nm optical pulses from the mode-lock laser are sent into a periodically-poled lithium niobate (ppLN) crystal waveguide to generate 775 nm optical pulses using second harmonic generation (pulse duration ~ 2 ps). Then the 775 nm optical pulses are coupled into a periodically-poled potassium titanyl phosphate (ppKTP) crystal waveguide with 10.5 mm length and $110 \mu\text{m}$, and 1550 nm photon pairs are generated through type-II spontaneous parametric down conversion. The spectral correlation between photon pairs can be neglected [S3]. As the generated photon pairs have orthogonal polarization, we use polarization beam splitter (PBS) to deterministically separate photons of each pair. Optical bandpass filters (OBPF) are used in both optical paths to ensure only photons with longer wavelength are coupled into the device, and only photons with shorter wavelength are coupled into the optical delay line (ODL). In the end, photons are coupled into a 50:50 beam splitter, and detected by two superconducting single-photon detectors (SSPD) in a cryostat cooled to 1.65 K [S4]. The photon incoming events of the two SSPDs are recorded by the time-correlated single photon counting unit (TCSPC). By comparing the arrival time list of the two SSPDs, we can identify the coincidence events from the correlated photon pairs. The coincidence rate is calculated based on a 256 ps binning of the photon arrival time. In the whole process, the 1550 nm optical pulses from the mode-lock laser are synchronized with the RF drive for the mechanical mode with the method shown in Fig. S1. Therefore, the photon pairs generated in ppKTP are also synchronized with the RF drive.

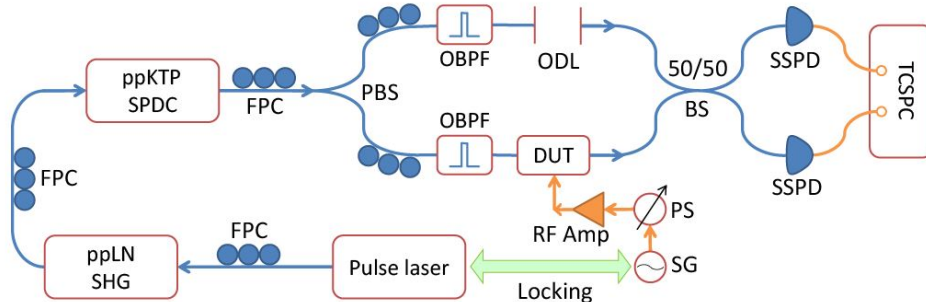


Figure S3. **Experimental setup for two-photon quantum interference with different colors.** ppLN, periodically poled lithium niobate; ppKTP, periodically poled potassium titanyl phosphate; FPC, fiber polarization controller; PBS, polarization beam splitter; OBPF, optical bandpass filter; ODL, optical delay line; BS, beam splitter; DUT, device under test; SSPD, superconducting single-photon detector; TCSPC, time-correlated single photon counting unit. RF Amp, RF amplifier; SG, signal generator; PS, phase shifter.

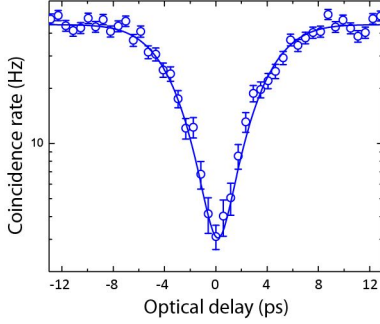


Figure S4. Coincidence rate between the two SSPDs using photon pairs with the same wavelength

We also performed the quantum interference experiment without the device. By tuning the wavelength of optical pulses from the mode-lock laser, photon pairs with the same wavelength can be generated. Using photon pairs with the same wavelength, we observe the maximum $V = (92.4 \pm 4.3)\%$ visibility of the coincidence rate (Fig. S4).

IV. PHOTON PROPAGATION LOSS IN THE FREQUENCY SHIFTER

The photon propagation loss in the frequency shifter consists of the intrinsic material loss and the scattering loss induced by waveguide pedestals. The intrinsic material loss of AlN waveguide is around 0.6 dB/cm, contributing 0.36 dB to the total propagation loss of the 6 mm long device [S5]. The scattering loss is less than 0.005 dB per pedestal, which is determined through finite-element simulations, thus the total scattering loss is less than 0.3 dB. As a result, the total propagation loss is less than 0.66 dB.

* hong.tang@yale.edu

[S1] Haus, H. A. Waves and fields in optoelectronics, Prentice Hall (1983).
 [S2] Schuck, C., Guo, X., Fan, L., Ma, X., Poot, M., & Tang, H. X. Quantum interference in heterogeneous superconducting-photonics circuits on a silicon chip. Nature Comm. 7, 10352 (2016).
 [S3] Eckstein, A., Christ, A., Mosley, P. J., & Silberhorn, C. Highly efficient single-pass source of pulsed single-mode twin beams of light. Phys. Rev. Lett. 106(1), 013603 (2011).
 [S4] Cheng, R., Guo, X., Ma, X., Fan, L., Fong, K. Y., Poot, M. & Tang H. X. Self-aligned multi-channel superconducting nanowire avalanche photodetector. arXiv:1601.01719 (2016).
 [S5] Xiong, C., Pernice, W. H., & Tang, H. X. Low-loss, silicon integrated, aluminum nitride photonic circuits and their use for electro-optic signal processing. Nano Lett. 12, 3562-3568 (2012).